N84-34025

DOE/JPL-956741-84/01

JPL NO. 9950-924

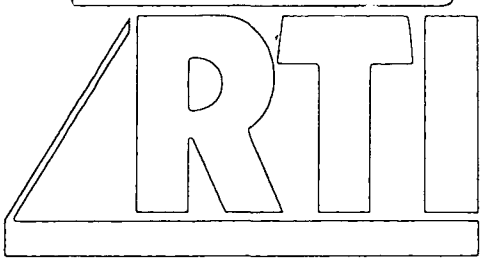

RESEARCH TRIANGLE INSTITUTE

June 1984

COMPREHENSIVE SILICON SOLAR CELL COMPUTER MODELING

Quarterly Progress Report No. 1

January 5, 1984, to April 4, 1984

M. F. Lamorte

Principal Investigator

JPL Contract No. 956741

RTI Project No. 415U-2850

POST OFFICE BOX 12194 RESEARCH TRIANGLE PARK, NORTH CAROLINA 27709

This work was performed for the Jet Propulsion Laboratory, California Institute of Technology, and was sponsored by the United States Department of Energy through an agreement with the National Aeronautics and Space Administration.

This report was prepared as an account of work sponsored by the United States Government. Neither the United States nor the United States Department of Energy, nor any of their employees, nor any of their contractors, subcontractors, or their employees, makes any warranty, expressed or implied, or assumes any legal liability or responsibility for the accuracy, completeness or usefulness of any information, apparatus, product or process disclosed, or represents that its use would not infringe privately owned rights.

TABLE OF CONTENTS

	Page
1.0 INTRODUCTION	1
2.0 DESCRIPTIONS OF THE INVESTIGATIONS CONDUCTED	4
2.1 Analytical Method Used to Represent Solar Cell Structures	4
2.2 Analytical Representations of Phenomena Submodels	5
2.2.1 Mobility	5
2.2.2 Diffusivities	11
2.2.3 Boundary Conditions at Depletion Region Edges	17
2.2.4 Boundary Conditions Imposed at the Mesh Points	23
2.2.5 Bandgap Narrowing and Intrinsic Concentration	24
2.2.6 Carrier Lifetime	30
2.2.6.1 Shockley-Read-Hall	30
2.2.6.2 Trap-Assisted Auger	34
2.2.6.3 Band-to-Band Auger	36
2.2.6.4 Composite Relationship	36
2.2.7 Induced Surface Electric Field Due to OCI	37
2.2.8 Built-In Fields - Low and High Injection Levels	40
3.0 SUMMARY	44
REFERENCES	45

ACKNOWLEDGEMENT

Coding of the solar cell analysis, debugging of the program, and other assistance was provided by W. M. Yeager and is gratefully acknowledged.

1.0 INTRODUCTION

This report summarizes the work conducted under this contract during the period of January 5, 1984, to April 4, 1984. Contract goals are to develop an efficient, comprehensive Si solar cell modeling program that has the capability of simulation accuracy of 5 percent or less.

Computer simulation programs, in general, may be subdivided into a number of major tasks: (1) analytical method used to represent the physical system; (2) phenomena submodels that comprise the simulation of the system; (3) coding of the analysis and the phenomena submodels; (4) coding scheme that results in efficient use of the CPU so that CPU costs are low; and (5) modularized simulation program with respect to structures that may be analyzed, addition and/or modification of phenomena submodels as new experimental data become available, and the addition of other photovoltaic materials. These tasks are briefly discussed below.

Computer modeling simulations have been shown to be very useful in the development of semiconductor devices in those cases where the simulation is an accurate representation of the physical device. However, to be an effective aid to the experimentalist and to become an equal partner in the technologies used in device development, it may be required to operate the computer program frequently each day in an active developmental program. For frequent use, as required in solar cell development, CPU costs must be low. Moreover, low CPU cost allows for engaging in computer experiments, which can be made to be a very useful and powerful technique.

Computer modeling using numerical integration methods in Si device technology have usually shown fair-to-good agreement with experimental data. However, CPU costs for the execution of computer programs that

are based on numerical integration methods are typically high for their use as a laboratory or manufacturing tool [1]. The number of bias points that are required to study optimized device designs is usually more than 1,000 to 2,000 runs. Similarly, a comprehensive study involving device structures or new types of devices typically exceeds 2,000 runs. In most cases, the cost of such modest studies for the benefits gained is not attractive. It is clear that conducting in-depth studies is not cost-effective; for this reason, numerical integration methods are not used for comprehensive studies.

A method has been developed that, in principle, should result in simulation accuracy equivalent to that demonstrated by numerical integration methods, but with low CPU costs. This method uses recursion relationships to solve for the constants of integration and is subsequently described.

Simulation accuracy is determined by both the accuracy of the analytical method representing the device and the accuracy of the phenomena submodels in representing the corresponding experimental data related to material properties. For most efficient use of the CPU, the accuracy of the analytical method and of the phenomena submodels should be equivalent. For example, even if the analytical method accurately represents the device, simulation results may not agree with experimental data if the phenomena submodels are accurately represented. The reverse is also true. In solar cells, the phenomena submodels that produce first-order effects in terminal characteristics are: absorption curve, built-in and induced electric fields, bandgap, lifetime, mobilities, diffusivities, photoexcited carrier concentrations, surface recombination velocities, junction transport, etc. Some of these will be discussed in this report. The representation of the phenomena submodels must take on an importance equal to the analytical method used to represent the system.

Codings of the analysis and phenomena submodels are separated in the program. Moreover, the coding of the submodels is modularized so that there is maximum flexibility to add, subtract, and/or modify them.

The efficiency of the coding may only be demonstrated by the accuracy of the simulation results with experimental data and the corresponding CPU execution time.

The spectrum of structures and cases that may be treated by the simulation program depends on the analytical method or algorithm used to represent the device, generality of the boundary conditions imposed, comprehensiveness of the phenomena submodels, and the generality of representation of each of the submodels. These issues will be described below.

2.0 DESCRIPTION OF THE INVESTIGATIONS CONDUCTED

2.1 Analytical Method Used to Represent Solar Cell Structures

RTI has been developing computer modeling programs for semiconductor devices since 1976 [2-9]. The major element that has evolved out of these modeling programs is the analytical method that is used to analyze physical systems. To obtain an accurate representation of a physical system, the system geometry is divided into a number of segments (mesh points). In a one-dimensional geometry, the segments are defined by a series of parallel planes. The separation of the planes defining the segments determines the simulation accuracy. The segments may be taken as thin as required to obtain the accuracy desired. The transport equations, governing the behavior of the physical system, are applied to each segment, and a closed-form solution is obtained in each of the segments. It has been demonstrated that when applying the boundary conditions to the solutions at each of the planes, there exists a recursion relationship between the constants of integration of the solutions obtained in each segment.

This method has been applied to semiconductor devices and has been shown to give excellent agreement with experimental results. It has been applied to devices for which the solutions are functions of position and time, such as photodiodes [8] and avalanche photodiodes (APD) [8]. The method has also been applied to solar cells, where the solutions are functions only of position [unpublished].

Convergence problems do not impose any conditions on the mesh point separation. The segments may be made arbitrarily thin or arbitrarily large. For maximum accuracy in simulating a physical system, a large number of segments may be required. The segments may be increased beyond 1,000 for greater accuracy; however, it has been found

that this is not always necessary. In the case of APDs, a device for which accuracy of representation is difficult, simulation results were studied for f = 2 up to f = 80 to determine the agreement between modeling and experimental data. It was found that the results obtained for f = 15 were within 1 percent of the results obtained for f = 80 [8]. This clearly shows these real advantages of the recursion relationship method over the numberical integration method: (1) a "guess solution" is not required; (2) convergence is always obtained for any number of mesh points; (3) a smaller number of mesh points may be used; (4) transport equations are solved by means of recursion relationships; and (5) CPU running time is reduced significantly.

During this contractual period, the analytical method described above has been applied to silicon solar cell structures; however, it has been generalized so that it may be applied to heterostructures encountered in amorphous silicon, III-V and II-VI material-based cells. Cascade cell structures may also be analyzed by means of this solution. The silicon solar cell structures that may be analyzed are given in Table 1, including the effect of an oxide-charged insulator (OCI).

Final results of the recursion relationships have not yet been obtained and will be reported in the second quarterly report.

2.2 Analytical Representations of Phenomena Submodels

In this section, a brief discussion is presented of some of the phenomena submodels and the representations used in the simulation program.

2.2.1 Mobility

Carrier mobilities in silicon have been studied by Dorkel and Leturcq [10], denoted DL mobility. They have assessed experimental and theoretical studies and developed analytical relationships which represent

Top \ Base	P	P^+	PP^+
n	•	•	•
n^+	•	•	•
n^+n	•	•	•

Table 1. Silicon structures that may be studied using the simulation program.

low field electron and hole mobility, depending on impurity concentration (ionized impurity scattering), temperature (lattice scattering), and injection level (carrier-carrier scattering). The DL mobility formulation has been selected as the primary method to be used in the simulation program, because the mobility components that arise from the three scattering phenomena are easily discerned. In addition, the composite form of the DL mobility relationships are relatively simple to apply, and it contains the mobility component arising from carrier-carrier scattering which becomes important in degenerate material and/or high injection levels. However, it appears that the DL relationships may not accurately represent mobility data for net impurity concentrations above 2-3 x 10^{18} cm^{-3} under low injection levels and for nonequilibrium values of the electron-hole product ($p_n n_n$ or $p_p n_p$) above 10^{36} cm^{-6}. This aspect will be dealt with subsequently.

The DL mobility relationships, which provide for silicon mobility dependency on impurity concentration, temperature and injection level are given by the expressions:

$$\mu_L = \mu_{LO}\left(\frac{300}{T}\right)^a \quad , \tag{1}$$

$$\mu_I = \frac{AT^{3/2}}{N\left[\ln\left(1 + \frac{BT^2}{N}\right) - \frac{BT^2}{N+BT^2}\right]} \quad , \tag{2}$$

$$\mu_{ccs} = \frac{2 \times 10^{17}\, T^{3/2}}{\sqrt{pn}\,\ln\left[1 + \frac{8.28 \times 10^{8} T^2}{(pn)^{1/3}}\right]} \quad , \tag{3}$$

$$X = \sqrt{6\frac{\mu_L(\mu_I + \mu_{ccs})}{\mu_I \mu_{ccs}}} \quad , \tag{4}$$

$$\mu = \mu_L \left[\frac{1.025}{1 + \left(\frac{X}{1.68}\right)^{1.43}} - 0.025 \right]. \qquad (5)$$

In the above set of equations, both electron and hole mobilities are represented and for which the baseline constants are listed in Table 2. Using these relationships, both electron and hole mobilities may be obtained in n-type material where N represents the net donor concentration, N_{DNet}. Similarly, electron and hole mobility may be determined in p-type using the appropriate mobility parameters in Table 2.

Eqs. (1), (2), and (3) represent the mobility components produced by lattice, ionized impurities, and carrier-carrier scattering. The latter is important in degenerate material and at high injection levels, and is usually negligible for most other cases. On the other hand, the lattice scattering and ionized impurity scattering are determined under conditions close to thermal equilibrium.

Lattice scattering mobility, Eq. (1), is produced by a scattering phenomenon attributed to accoustic phonons. This component decreases with increasing temperature, and the parameters, μ_{LO} and "a," depend on the carrier type and the temperature range. It is this component which, in large measure, determines the temperature behavior of mobility. It is clear from Table 2 that $\mu_{LNO} > \mu_{LPO}$.

Ionized impurity scattering mobility, Eq. (2), is produced because of scattering of carriers by immobile ionized impurities. This mobility decreases with increasing impurity concentration or decreasing temperature. Implicit in this formulation is that the effect of scattering is the same for electrons and holes in the presence of ionized donors as well as for ionized acceptors.

Parameter	Electrons	Holes
μ_{Lo}	1430 cm^2 $(V\ sec)^{-1}$	495
a	2.2	2.2
A	4.61×10^{17} $(cm\ V\ sec\ K^{3/2})^{-1}$	1×10^{17}
B	1.52×10^{15} $cm^{-3}\ K^{-2}$	6.25×10^{14}

Table 2. Baseline values of mobility parameters using the Dorkel-Leturcq [10] representation.

Carrier-carrier scattering mobility, Eq. (3), becomes important where the electron-hole product is greater than 10^{28} cm^{-6} for 10^{14} cm^{-3} impurity concentration and when the product is greater than 10^{32} cm^{-6} for 10^{19} cm^{-3} impurity concentration. These conditions occur for injection levels produced under solar concentrations exceeding 10 to 20 suns.

Electron mobilities predict experimental values to within 5 percent in the temperature range above 200 K, and for doping levels less than 3×10^{18} cm^{-3}. At 300 K, hole mobilities are predicted to within 5 percent or less, and for doping concentration less than 2×10^{18} cm^{-3}. There is agreement with experimental data in the temperature range 200 to 300 K. However, hole mobility data above 300 K and the DL mobility relationships cannot be assessed at this time [10].

Due to limitations of applicability of the DL formulation in some temperature and doping concentration ranges, a second representation has been included in the mobility submodel. This representation is due to Arora et al. [11]. It is denoted as the AHR mobility formulation.

Composite mobility relationships for electrons and holes have been obtained empirically, as a function of temperature (lattice scattering mobility) and impurity concentration (ionized impurity scattering mobility), based on experimental data and the Brooks-Herring theory of mobility. The relationships predict electron and hole mobility to within ±13 percent up to 10^{20} cm^{-3} doping concentration and in the 250 to 500 K temperature range. The relationships are given by:

$$\mu_n = 88\left(\frac{300}{T}\right)^{0.57} + \frac{7.4 \times 10^8 \left(\frac{1}{T}\right)^{2.33}}{1 + \frac{0.88N}{1.26 \times 10^{17}} \left(\frac{300}{T}\right)^{2.546}} , \qquad (6)$$

$$\mu_p = 54.3 \left(\frac{300}{T}\right)^{0.57} + \frac{1.36 \times 10^8 \left(\frac{1}{T}\right)^{2.33}}{1 + \frac{0.88N}{2.35 \times 10^{17}} \left(\frac{300}{T}\right)^{2.546}} \quad . \quad (7)$$

The above formulation may be used in those temperature and doping concentration values where the DL formulation exhibits a poor representation of experimental data. However, Eqs. (6) and (7) only apply to low injection level cases, in which case we will resort to the DL formulation.

The DL [10] and AHR [11] relationships are compared in the impurity concentration range of 10^{14} to 10^{19} cm^{-3} in Figures 1, 2, and 3 for 200, 350, and 500 K, respectively, under low injection level, $pn = 10^{26}$ cm^{-3}. Agreement for electron mobility between the formulations is excellent at 350 and 500 K and not as good at 200 K. The overall agreement for holes is not as good as it is for electrons. However, these results show that either formulation may be used to represent mobility data under low injection levels.

2.2.2 Diffusivities

In most cases, the carrier diffusivities used are of the Einstein form represented for electrons by

$$D_{no} = \frac{kT}{q} \mu_n \quad . \quad (8)$$

However, in degenerate and/or high injection levels, the Einstein relationship is a poor approximation.

Consider a degenerate p-type semiconductor under thermal equilibrium (i.e., open-circuit conditions) as shown in Figure 4(a). Under these conditions, the electron current, given by

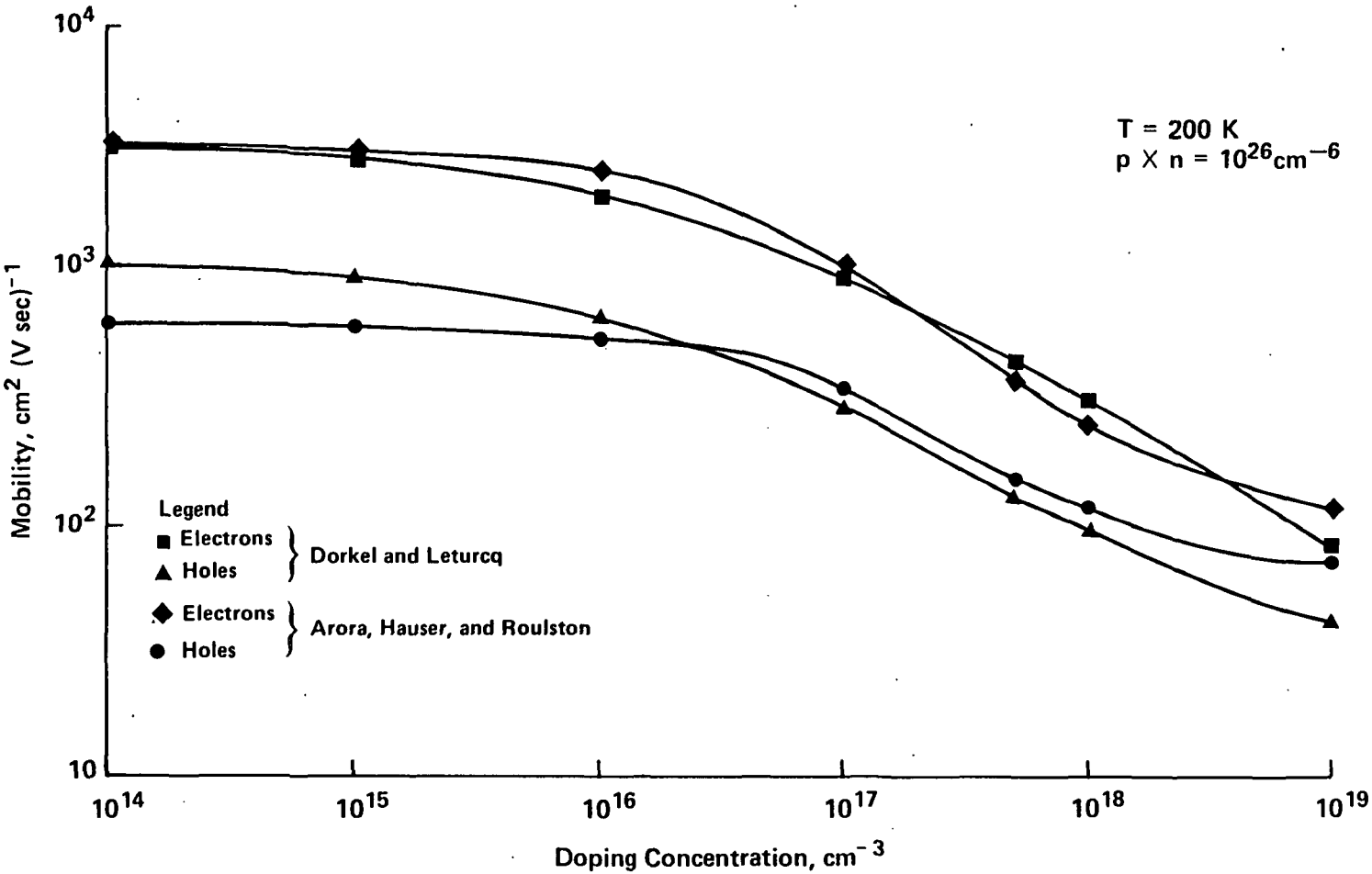

Figure 1. Comparison between the DL and AHR relationships for electron and hole mobility at 200 K under low injection level.

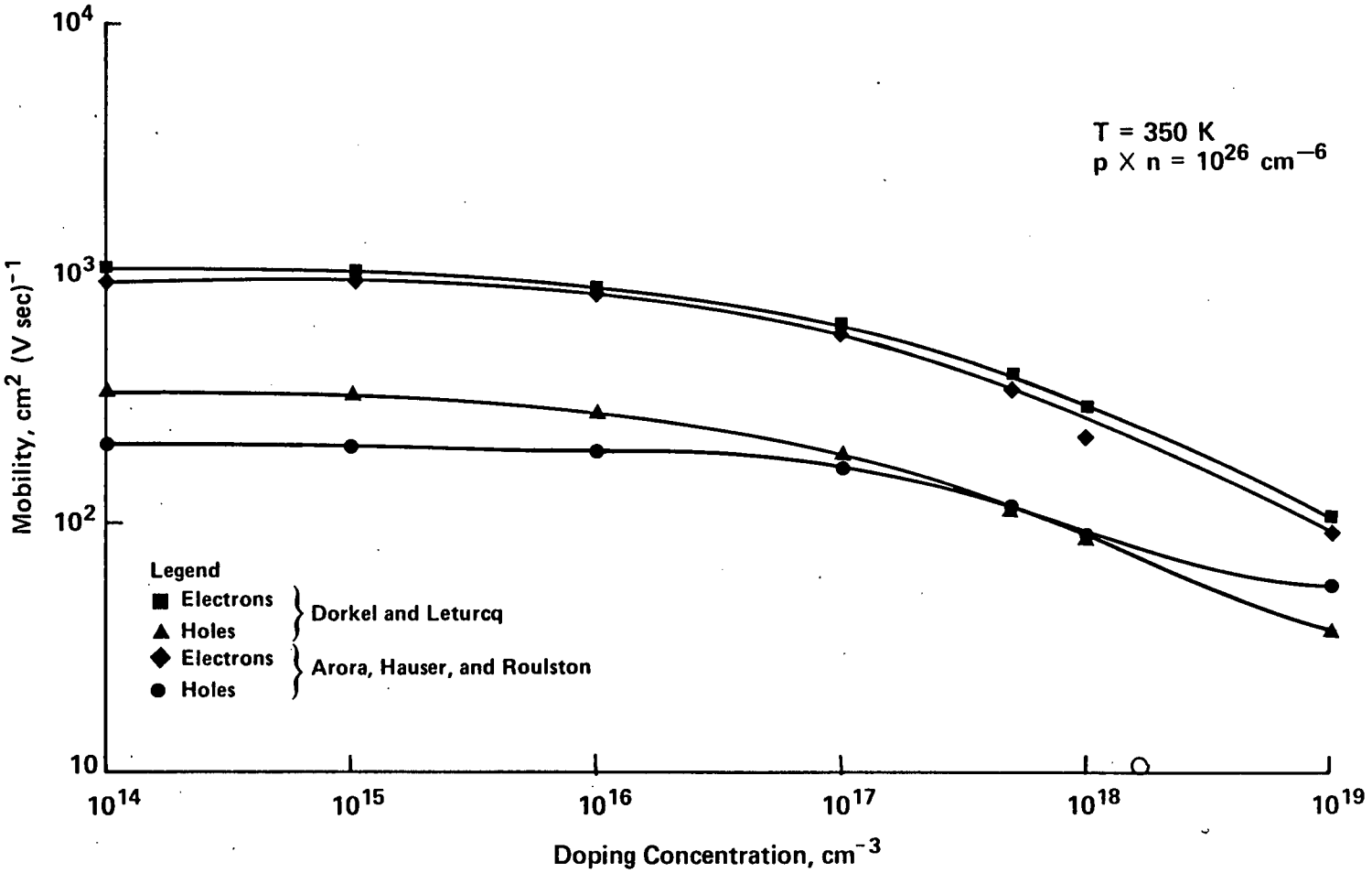

Figure 2. Comparison between the DL and AHR relationships for electron and hole mobility at 350 K under low injection level.

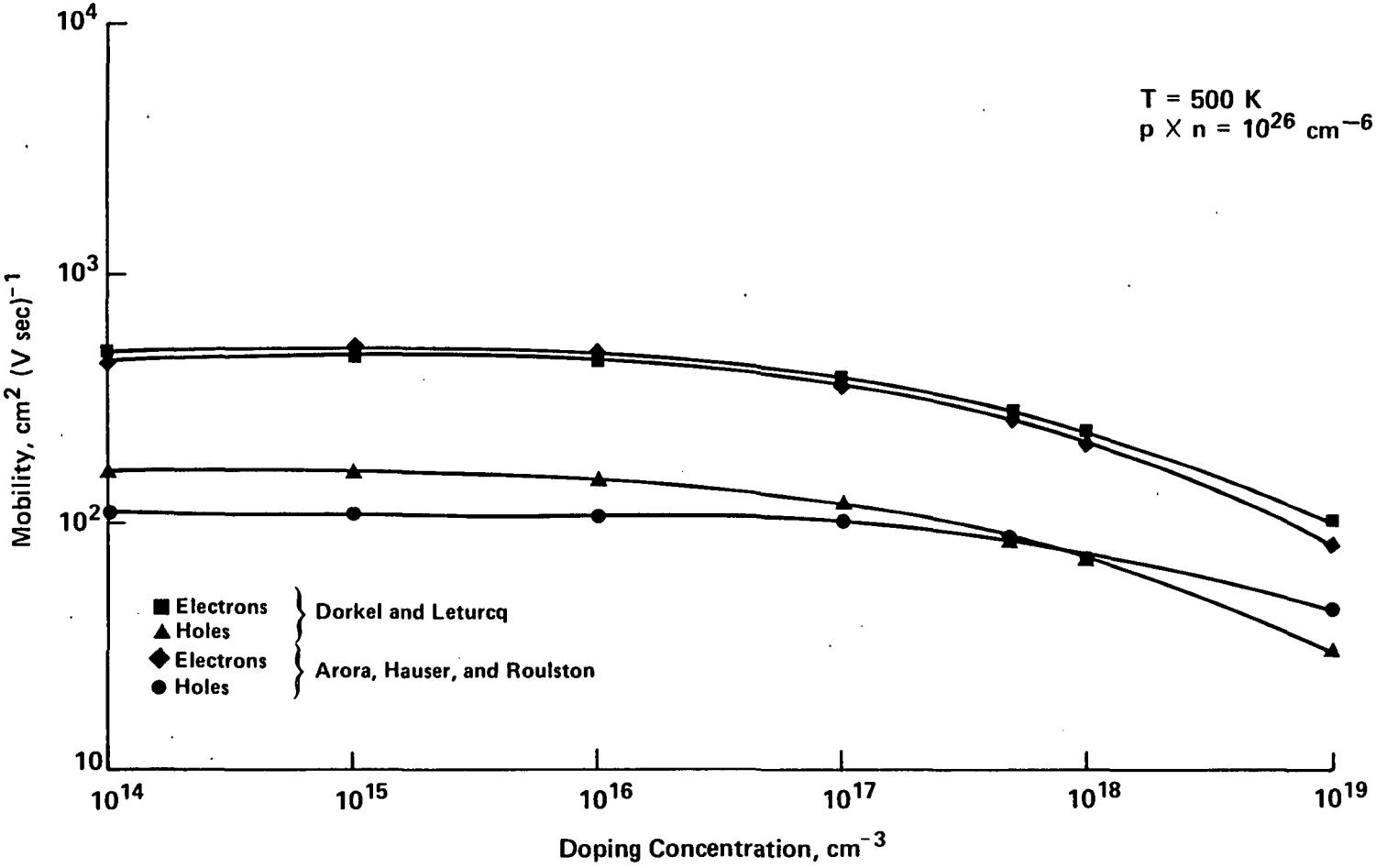

Figure 3. Comparison between the DL and AHR relationships for electron and hole mobility at 500 K under low injection level.

$$J_n = q\,\mu_n\,n_{po}\,E_x + q\,D_n\,\frac{dn_{po}}{dx} \quad , \tag{9}$$

is zero, from which the electron diffusivity is given by

$$D_n = -\frac{\mu_n n_{po} E_x}{\frac{dn_{po}}{dx}} \quad . \tag{10}$$

E_x in this case is the built-in potential that is established to produce an equal, but opposite drift current to the diffusion current. The built-in field is obtained from a relationship for the conduction bandedge, E_c. The bandedge expression may be placed in a form given by

$$E_c = -\psi + \text{constant} \tag{11}$$

where ψ is the electrostatic potential. The built-in potential is obtained from Eq. (11), represented by

$$E_x = \frac{dE_c}{dx} = -\frac{d\psi}{dx} \quad . \tag{12}$$

To obtain dn_{no}/dx, we use the relationship

$$\frac{dn_{po}}{dx} = \frac{\partial n_{po}}{\partial E_c}\,\frac{dE_c}{dx} \quad ; \tag{13}$$

and substituting from Eq. (12), the result is

$$\frac{dn_{po}}{dx} = E_x\,\frac{\partial n_{po}}{\partial E_c} \quad . \tag{14}$$

The relationship for electron concentration (using the rigid band approximation) given by

$$n_{po} = N_c F_{1/2}(\eta_o) \tag{15}$$

where N_c is the density-of-states at the conduction bandedge, $F_{1/2}$ is the Fermi-Dirac integral of 1/2-order, and

$$\eta_o = q \frac{E_{Fo}-E_c}{kT} \tag{16}$$

is the argument for thermal equilibrium. Using the relationship

$$\frac{\partial n_{po}}{\partial E_c} = N_c \frac{\partial \eta_o}{\partial E_c} \frac{\partial}{\partial \eta_o} [F_{1/2}(\eta_o)] \quad , \tag{17}$$

it can be shown then [12] that

$$\frac{\partial}{\partial \eta_o} [F_{1/2}(\eta_o)] = F_{-1/2}(\eta_o) \quad , \tag{18}$$

where $F_{-1/2}(\eta_o)$ is the Fermi-Dirac integral of the -1/2-order. Substituting Eqs. (14), (15), (16), (17), and (18) into Eq. (10) results in the electron diffusivity in degenerate material given by

$$D_n = D_{no} \frac{F_{1/2}(\eta_o)}{F_{-1/2}(\eta_o)} \quad . \tag{19}$$

A similar procedure and relationship may be obtained for the case of high injection level, by elevating temperature or by another method in which the same electron-hole pair concentration is produced as through

irradiation by a high photon flux as shown in Figure 4(b) under dynamic equilibrium and open-circuit conditions. The latter assumes that a uniform distribution of electron-hole pairs is generated. The diffusivity is given by

$$D_n = D_{no} \frac{F_{1/2}(\eta_n)}{F_{-1/2}(\eta_n)} \quad , \tag{20}$$

for which

$$\eta_n = q \frac{E_{Fn} - E_c}{kT} \quad , \tag{21}$$

where E_{Fn} is the quasi-Fermi level for electrons. Under thermal equilibrium conditions, Eq. (20) reduces to the relationship given in Eq. (19). Corresponding relationships exist for holes.

Figure 5 shows the electron and hole diffusivities, normalized with respect to the Einstein diffusivity, plotted as a function of their respective arguments (η and $-\varepsilon_G-\eta$) which contain the Fermi level. Increasingly positive arguments represent increasing degeneracy for which the diffusivities show significant increases. Negative arguments represent nondegenerate cases where the diffusivity ratios approach unity. For argument values of +10, the diffusivity ratios are greater than six. This represents a condition where the Fermi level penetrates the corresponding bands by 0.15 eV, which are attained for 10^{20} cm^{-3} doping under low injection. High injection adds to this penetration, and the diffusivity ratio increases still further.

2.2.3 Boundary Conditions at Depletion Region Edges

Boundary conditions imposed at depletion region edges are briefly discussed below. Due to the controversy that may surface when

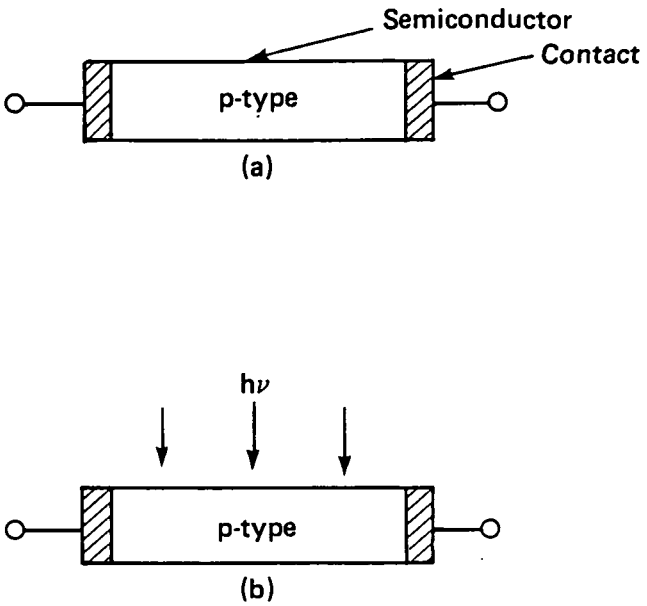

Figure 4. Physical systems used to describe carrier diffusivities: (a) degenerate semiconductor in thermal equilibrium; and (b) degenerate and/or high injection level in a semiconductor in dynamic equilibrium.

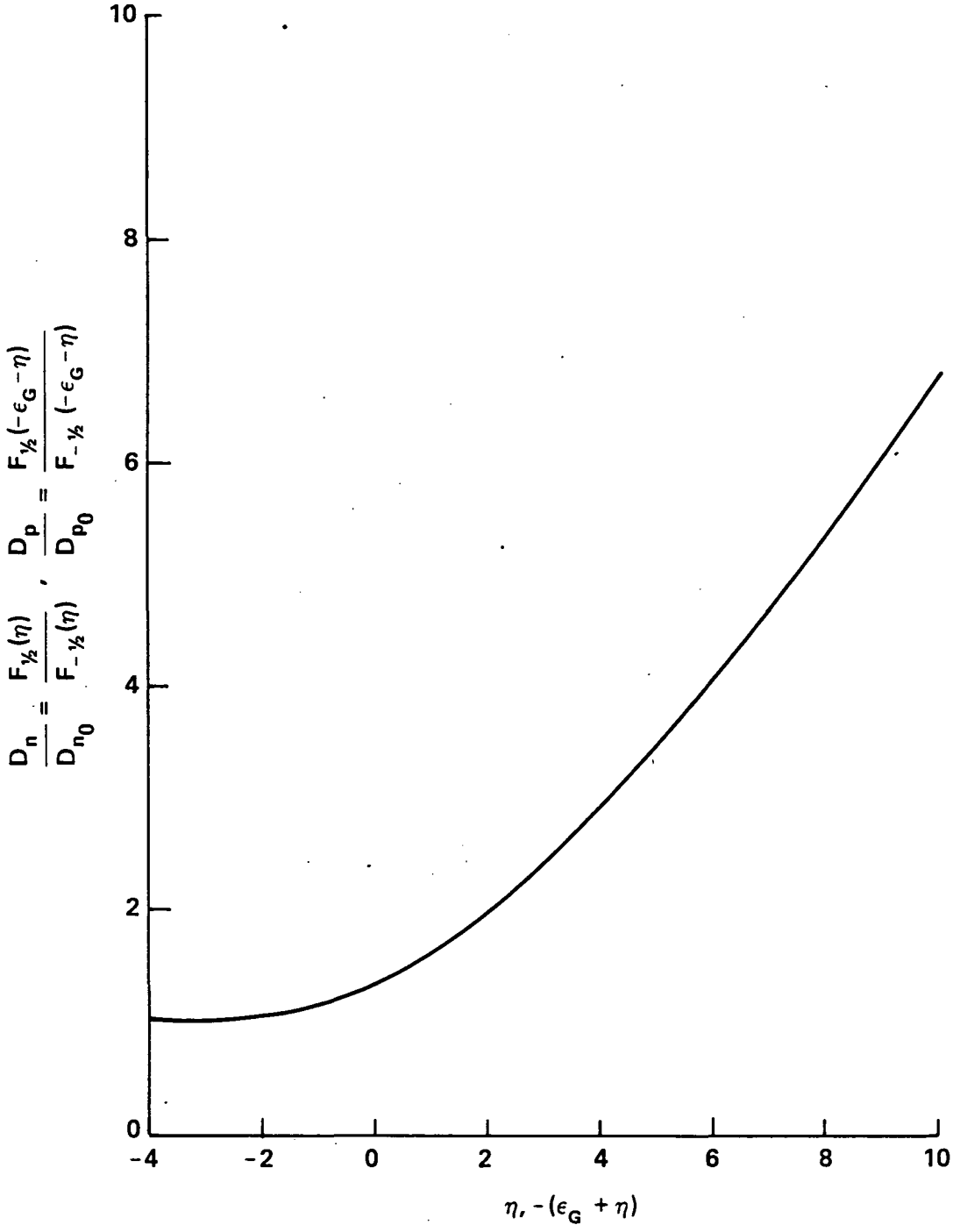

Figure 5. Electron and hole diffusivities normalized with respect to the Einstein relationship for degenerate and/or high injection level conditions for all temperatures.

discussing these boundary conditions under high injection levels, special attention was devoted to this subject [13-19]. During the course of this investigation, a number of significant results were obtained, and these will also be presented below.

Consider the geometry where x_2 and x_3 denote the depletion region edges in the n- and p-regions, respectively. The symbols for the corresponding carrier concentrations are denoted $p_n(x_2)$, $n_n(x_2)$, $p_p(x_3)$, and $n_p(x_3)$. In general, the relationships that exist between these concentrations are given by

$$p_n(x_2) = p_p(x_3)\, e^{-\frac{qV_{bi}}{kT}} , \tag{22}$$

for holes, and for electrons by

$$n_p(x_3) = n_n(x_2)\, e^{-\frac{qV_{bi}}{kT}} , \tag{23}$$

where V_{bi} is the nonequilibrium built-in potential established in the depletion region. While the expressions in Eqs. (22) and (23) are valid for both equilibrium and nonequilibrium conditions, at high injection levels the quantities $p_p(x_3)$ and $n_n(x_2)$ are unknown. This gives rise to two different forms of the boundary conditions for low and high injection levels. The different forms are a direct result of the charge neutrality conditions that exist under low level injection, given by

$$n_n(x_2) \rightarrow n_{no}(x_2) = N_D(x_2) \tag{24}$$

in the n-region, and in the p-region by

$$p_p(x_3) \rightarrow p_{po}(x_3) = N_A(x_3) \quad , \tag{25}$$

where $N_D(x_2)$ and $N_A(x_3)$ represent donor and acceptor concentrations in the n- and p-type regions, respectively, at the depletion edges. Substituting Eq. (24) into Eq. (23), and Eq. (25) into Eq. (22), gives the boundary conditions for low injection level:

$$p_n(x_2) = p_{po}(x_3)\, e^{-\frac{qV_{bi}}{kT}} \quad , \tag{26}$$

and

$$n_p(x_3) = n_{no}(x_2)\, e^{-\frac{qV_{bi}}{kT}} \quad . \tag{27}$$

The nonequilibrium built-in potential is defined by

$$V_{bi} = V_{bio} - V_J \quad , \tag{28}$$

where V_{bio} is the built-in potential at thermal equilibrium, and V_J is the photovoltage. Therefore, under low injection levels, $p_n(x_2)$ and $n_p(x_3)$ may be determined.

In the high injection case, the charge neutrality condition imposed in the n-region is given by

$$n_n(x_2) - p_n(x_2) = N_D(x_2) \tag{29}$$

and in the p-region by

$$p_p(x_3) - n_p(x_3) = N_A(x_3) \quad , \tag{30}$$

where $p_n(x_2)$ may be comparable to or even greater than $N_D(x_2)$ and similarly for $n_p(x_3)$ and $N_A(x_3)$. One form of the boundary condition under high injection was first reported by Fletcher [14] and given by

$$p_n(x_2) = \frac{[N_A(x_3) + N_D(x_2)\,\xi\,]\,\xi}{1-\xi^2} \tag{31}$$

for holes at x_2 and by

$$n_p(x_3) = \frac{[N_D(x_2) + N_A(x_3)\,\xi\,]\,\xi}{1-\xi^2} \tag{32}$$

at x_3, where

$$\xi \equiv \frac{n_{ie}(x_2,T,N_D)n_{ie}(x_3,T,N_A)}{N_A(x_3)N_D(x_2)}\, e^{\frac{qV_J}{kT}} \quad . \tag{33a}$$

The quantity V_J is the photovoltage generated across the depletion region, x_3-x_2. The form of ξ is somewhat different from the results obtained in the literature because it includes the effects of bandgap narrowing through the intrinsic concentrations $n_{ie}(x_2,T,N_D)$ and $n_{ie}(x_3,T,N_A)$. To show this more explicitly, Eq. (33a) may be placed in the following form:

$$\xi \equiv \frac{n_{io}^2(T)e^{[\Delta E_G(x_2) + \Delta E_G(x_3)]/2kT}}{N_A(x_3)N_D(x_2)}\, e^{\frac{qV_J}{kT}} \quad . \tag{33b}$$

This form shows that ξ is dependent on the sum of the bandgap narrowing of the depletion edges. If the doping concentration at x_2 and x_3 are

1×10^{18} cm^{-3}, the sum of the bandgap narrowing is 0.086 eV and ξ is increased by a multiplicative factor of 28 compared to pure material.

An alternative form of these boundary conditions is attributed to Misawa [13]. While the Fletcher formulation is based on quantities defined at the depletion region edges (x_2 and x_3), the Misawa formulation also includes quantities defined at the outer boundaries of the n- and p-regions, which represent the ohmic contact interfaces ($x = 0$ and x_5) in a solar cell structure. The two relationships are given by

$$p_n(x_2) = p_{po}(x_5) e^{-\frac{q}{kT}\left[V(x_2) - V(x_5) + \int_{x_3}^{x_5} \frac{J_p}{q\mu_p p_p} dx\right]} , \quad (34)$$

and

$$n_p(x_3) = n_{no}(0) e^{-\frac{q}{kT}\left[V(0) - V(x_3) + \int_{0}^{x_2} \frac{J_n}{q\mu_n n_n} dx\right]} , \quad (35)$$

where $p_{po}(x_5)$ and $n_{no}(0)$ are the acceptor and donor concentrations at the ohmic contacts, and $V(x_5)$ and $V(0)$ are the corresponding potentials. The disadvantage of the Misawa form is the photocurrent J_p and J_n are required to be known in order to calculate $p_n(x_2)$ and $n_p(x_3)$.

2.2.4 Boundary Conditions Imposed at the Mesh Points

The analytical method described in Section 2.1 solves, in closed form, for the minority carrier concentrations at each mesh point. Therefore, each of the closed form solutions contains two constants of integration, which solutions must be obtained through the imposition of boundary conditions of each of the mesh points.

In the n-region, the boundary conditions at the j^{th} mesh point are:

$$p_{nej}(y_{oi}) = p_{ne(j+1)}(0)e^{(\Delta E_{vj}/kT)} \quad , \tag{36}$$

and

$$J_{pj}(y_{oj}) = J_{p(j+1)}(0) \quad , \tag{37}$$

where $p_{nej}(y_{oj})$ and $p_{ne(j+1)}(0)$ represent the photoexcited hole concentration, $J_{pj}(y_{oi})$ and $J_{p(j+1)}(0)$ the hole current density, y_{oi} the separation between the j^{th}-1 and j^{th} mesh point, and ΔE_{vj} the discontinuity in the valence bandedge. If $\Delta E_{vj} > 0$, a discontinuity in hole concentration exists and provides for carrier confinement. A corresponding set of conditions are imposed in the p-region.

2.2.5 Bandgap Narrowing and Intrinsic Concentration

Bandgap reduction has been shown to occur in silicon with increasing impurity concentration, which is attributed to the broadening of impurity levels and which ultimately overlap with the conduction and bandedges when donors and acceptors, respectively, are involved. This effect is well established from the results of band structure analysis [20-22], and has been shown by direct means through the measurement of the intrinsic optical absorption threshold [23]. The largest narrowing observed is 0.068 eV, using this technique, in n-type silicon for a donor concentration of 9×10^{19} cm^{-3} [23]. These experimental results were employed to develop models by a number of investigators to obtain

improved agreement between experimental data and theoretical calculations related to effects produced by high impurity concentrations in the emitter and base regions of bipolar transistors [24-26].

More recently, other methods have been used to measure bandgap narrowing [27,28]. These data have been analyzed and empirical relationships obtained which describe the bandgap and bandgap narrowing with increased impurity concentration and which are denoted here as the SD [27] and D [29] relationships. In most cases, the experimentally determined bandgap narrowing in the 10^{17} to 2×10^{19} cm^{-3} range is greater than the values resulting theoretical analysis [30-32]. The Slotboom and de Graaff (SD) values have been used to calculate injected electron current under contacts in logic circuits [33,34], to obtain improved agreement in calculating built-in potentials [35], and to model solar cells [36]. The results appear to be more encouraging for the SD than for the D relationships; therefore, in the following discussion the SD results are used.

Slotboom and de Graaff measure the bandgap by two indirect methods that involve the I_C-V_{EB} characteristic in NPN bipolar transistors, as a function of impurity concentration (4×10^{15} to 2.5×10^{19} cm^{-3}) and temperature (150 K to 400 K). Following MacFarlane et al. [37], a linear approximation is assumed for the bandgap above 250 K and represented by

$$E_G(T,N) = E_{GO} - \alpha T - \Delta E_G(N) \quad , \tag{38a}$$

where $\alpha = 3.855 \times 10^{-4}$ $eV(K)^{-1}$ is the temperature coefficient, $E_{GO} = 1.206$ eV is a constant, and $\Delta E_G(N)$ is the bandgap narrowing. Both E_{GO} and α are independent of impurity concentration and temperature, while $\Delta E_G(N)$ is

dependent only on the net impurity concentration. If the bandgap, $E_G(T,N)$, is measured, the bandgap narrowing may be determined from the relationship

$$\Delta E_G(N) = E_{GO} - 3.855 \times 10^{-4}T - E_G(T,N) \quad . \tag{38b}$$

In analogy with nondegenerate material, Slotboom and de Graaff use the relationship

$$n_{ie}^2(T,N) = N_c N_v e^{-E_G(T,N)/kT} \tag{39}$$

to calculate $E_G(T,N)$ once they obtain $n_{ie}^2(T,N)$ from the measurement of collector current. N_c and N_v are the density of states at the conduction and valence bandedges, respectively, and are assumed to be invariant in form and in their values from those in pure silicon. These assumptions constitute what is commonly referred to as the Rigid Band approximation, because the assumptions are equivalent to assuming that the bandedges remain parabolic even in degenerate cases. Although this is almost certainly not true, it still represents an approximation that is more realistic than the estimates that are required in the bandstructure calculations [20-22]. As a result, Eq. (39) may be written in the form

$$n_{ie}^2(T,N) = n_{io}^2(T)e^{\Delta E_G/kT} \quad , \tag{40}$$

where the square of the intrinsic concentration in nondegenerate material is given by

$$n_{io}^2(T) = 9.6 \times 10^{32} T^3 e^{-E_{Go}/kT} \quad . \tag{41}$$

Slotboom and de Graaff state that their data demonstrates that $\Delta E_G(N)$ is independent of temperature. Therefore, they measured $n_{ie}(T,N)$ only at 300 K over a range of impurity concentration values. It is then assumed that the form of Eq. (40) applies to the doping and temperature studied. An empiracle relationship is obtained to represent bandgap narrowing and is given by

$$\Delta E_G(N) = 9 \times 10^{-3} \left[\ln \frac{N}{10^{17}} + \sqrt{\left(\ln \frac{N}{10^{17}} \right)^2 + \frac{1}{2}} \right] \text{eV} \quad . \quad (42)$$

Substituting for net concentration values, N gives the bandgap narrowing obtained from the measurement of $n_{ie}(T,N)$.

The Slotboom-de Graaff assumptions may be questioned. Although they have maintained electron injection into the degenerate base region at a low level, they claim that this is reason enough to represent the pn-product by Boltzmann statistics. The temperature behavior of hole mobility in the base region is determined by measuring the sheet resistance of the base region. This hole mobility temperature dependency is then ascribed for electrons as well. Moreoever, the temperature dependency of bandgap narrowing is inferred to be constant as a result of measuring the temperature behavior of the emitter-base voltage (V_{EB}) and of the electron mobility. The validity of the above assumptions is not questioned in general, but only as it applies to determining small effects such as bandgap narrowing.

A more realistic method to determine $\Delta E_G(N)$ from measured values of $n_{ie}(T,N)$ is to use Fermi-Dirac statistics when studying effects in degenerate materials. In the following, we present the results of a study that applies Fermi-Dirac statistics to bandgap narrowing. In

place of Eqs. (39)-(42), we substitute the relationship that applies to degenerate and nondegenerage cases given by [12]:

$$n_{ie}^2(T,N) = n_{io}^2 \frac{F_{1/2}(\eta)F_{1/2}(-\varepsilon_G-\eta)}{F_{1/2}(\eta_i)F_{1/2}(-\varepsilon_G-\eta_i)} \quad , \tag{43}$$

where $F_{1/2}(x)$ represents the Fermi-Dirac integrals of the 1/2-order, and

$$\eta = \frac{E_F-E_C}{kT} \quad , \tag{44}$$

$$\eta_i = \frac{E_{Fi}-E_C}{kT} \quad , \tag{45}$$

$$\varepsilon_G = \frac{E_c-E_v}{kT} \quad . \tag{46}$$

E_F, E_{Fi}, E_c, and E_v are used to represent the usual parameters.

The bandgap value, $E_G(T,N)$, is determined by substituting the Slotboom-de Graaff experimentally determined values of $n_{ie}(T,N)$, and the calculated values of $n_{io}(T)$ and η_i into Eq. (43) through a computer subroutine that requires that the relationship be satisfied. $E_G(T,N)$ is determined by this method over 1 x 10^{16} to 3 x 10^{19} cm^{-3} concentration range and 250 to 500 K temperature range, where the invariance of $\Delta E_G(N)$ with temperature is also assumed. The bandgap narrowing obtained from the two methods (SD method and the method used in this study) using Eq. (38b) are shown in Figure 6. These results show that for concentration values less than 1 x 10^{18} cm^{-3}, both methods give identical results over the temperature range. However, the method based on Fermi-Dirac statistics (F-D) results in larger bandgap narrowing values compared to the results based on Boltzmann statistics (B), and the difference increases with increasing concentration values. Even though the experimental values of

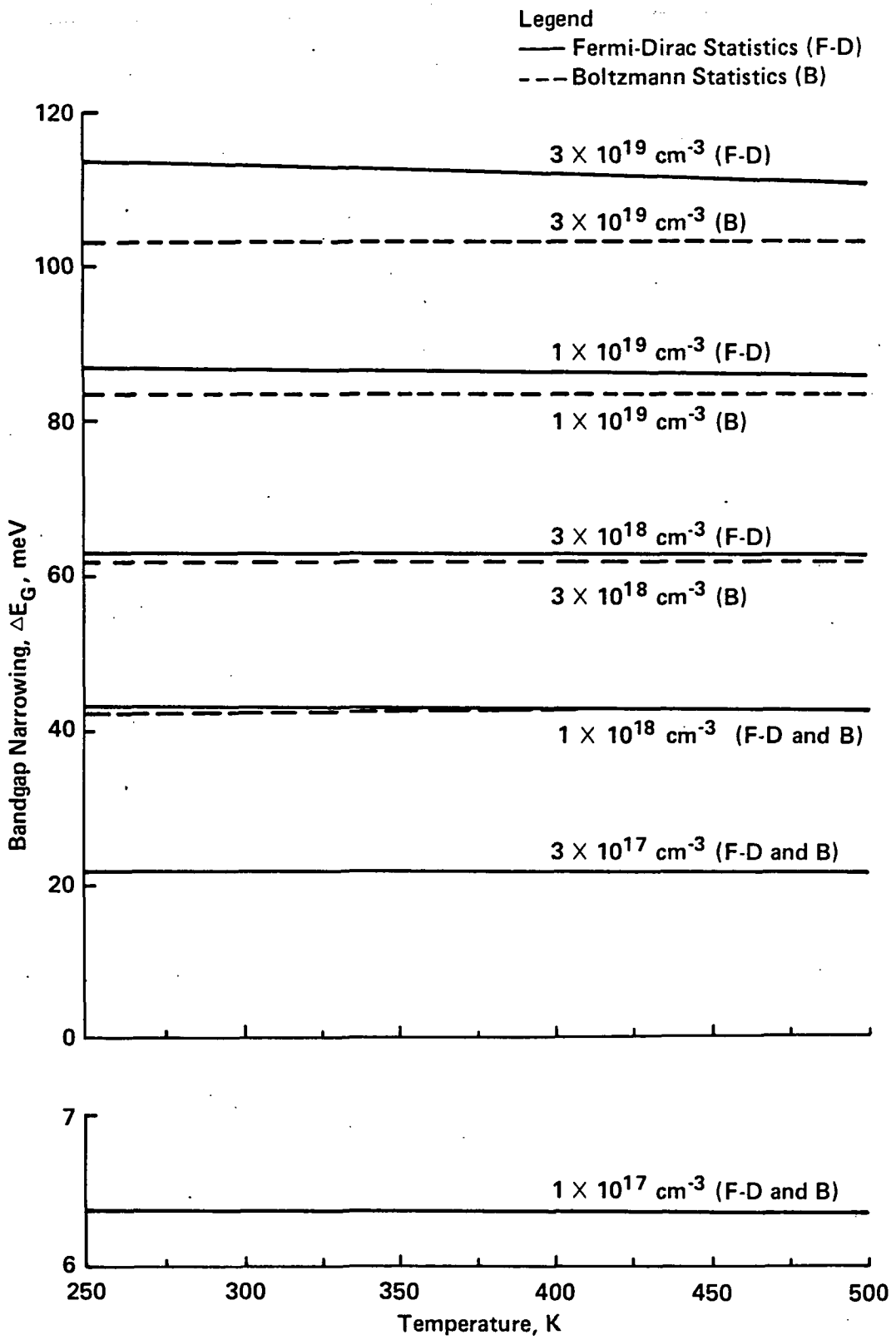

Figure 6. Bandgap narrowing calculated using Fermi-Dirac and Boltzmann statistical forms, and based upon n_{ie} (T,N) calculations using the Slotboom and deGraaf data at 300 K.

$n_{ie}(T,N)$ obtained by Slotboom and de Graaff for which $\Delta E_G(N)$ is independent of temperature, the F-D method nevertheless shows that $\Delta E_G(N)$ does exhibit a temperature dependency. Figure 7 shows the intrinsic concentration, $n_{ie}(T,N)$, versus 1/T for three concentration values. It is seen that $n_{ie}(T,N)$ is higher by approximately one decade for 3×10^{19} cm^{-3} compared to 1×10^{17} cm^{-3}.

2.2.6 Carrier Lifetime

It is well known that carrier lifetime plays a major role in obtaining high efficiency in silicon solar cells. As a result, a number of studies are contemplated that involve effects produced by the lifetime behavior which have not yet been resolved. For these reasons, composite lifetime relationships have been incorporated as submodels in the computer simulation program. The composite relationships contain recombination terms representing the Shockley-Read-Hall, trap-assisted Auger, and band-to-band Auger processes.

2.2.6.1 Shockley-Read-Hall (SRH)

Recombination processes that apply at low injection levels are referred to as the Shockley-Read-Hall (SRH) recombination [40,41]. This recombination relationship may also be applied to Auger recombination through trap-assisted processes. In silicon, the latter is most important, because silicon is characterized by indirect optical transitions.

The SRH recombination-generation relationship, which involves the electron and hole capture and emission at low injection levels through a single trap level, is given by [40,41]:

$$R_{SRH} = \frac{p_n - n_{ie}^2}{\tau_p[n+n_{ie}e^{(E_t-E_{Fi})/kT}] + \tau_n[p+n_{ie}e^{-(E_t-E_{Fi})/kT}]} \quad . \qquad (47)$$

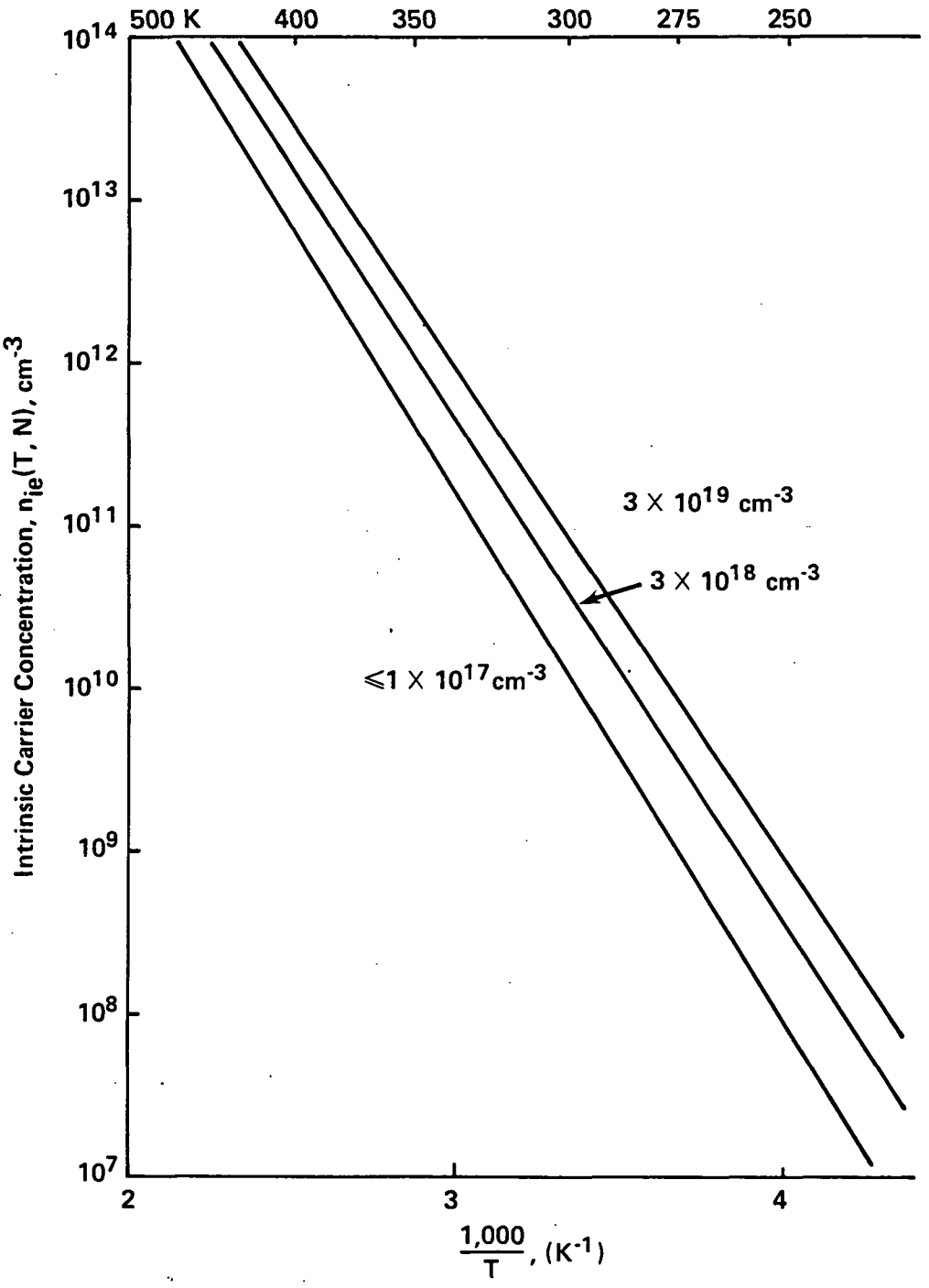

Figure 7. Curves representing calculations of the intrinsic concentration, $n_{ie}(T,N)$, based upon the Slotboom and de Graaff data.

The minority carrier lifetimes (τ_p and τ_n), carrier concentrations (p and n), intrinsic concentration (n_{ie}), trap energy level (E_t), and the intrinsic Fermi level (E_{Fi}) may all be sensitive to position, temperature, impurity concentration, and, for a number of these parameters, to injection level.

Kendall [38] has shown that experimental hole lifetime in as-grown n-type silicon ingots may be described by the expression

$$\tau_p(N_D) = \frac{\tau_{po}}{1 + \frac{N_D}{N_{Do}}} \quad , \tag{48}$$

where $N_D(x)$ is the donor concentration which may be position-dependent. The parameter τ_{po} is the lifetime in material for which $N_D << N_{Do}$, and N_{Do} is the threshold of donor concentration where recombination concentration begins to increase significantly. These parameters are listed in Table 3. By analogy, Fossum [39] has assumed a similar relationship for electrons given by

$$\tau_n(N_A) = \frac{\tau_{no}}{1 + \frac{N_A}{N_{Ao}}} \quad , \tag{49}$$

where τ_{no} and N_{Ao} have similar meanings as in Eq. (48). In those regions for which N_D and N_A are position-sensitive, the minority carrier lifetime will also be position-dependent.

Eqs: (48) and (49) may be made more general where the form of the relationships of τ_{po} and τ_{no} are given by

$$\tau_o = \frac{1}{\sigma v_{th} \frac{N_{to}}{2}} \quad . \tag{50}$$

Table 3. Summary of lifetime constants.

Parameter	Electrons: p-type	Holes: n-type
τ_{no}, τ_{po}	1.70×10^{-5} sec [39]	3.95×10^{-4} sec [39]
N_{Ao}, N_{Do}	7.10×10^{15} cm^{-3} [39]	7.10×10^{15} cm^{-3} [39]
$\sigma_n(300\ K)$, $\sigma_p(300\ K)$	5.9×10^{-16} cm^{-2}	2.2×10^{-16} cm^{-2}
$v_{thn}(300\ K)$, $v_{thp}(300\ K)$	1.09×10^{7} cm S^{-1}	1.52×10^{7} cm S^{-1}
N_{tpo}, N_{tno}	1.829×10^{13} cm^{-3}	1.514×10^{12} cm^{-3}
b_n, b_p	3.4 [42]	2.7 [42]
B_n, B_p	2.8×10^{-31} cm^{6} sec^{-1} [42,48,51,52]	0.99×10^{-31} cm^{6} sec^{-1} [42,48,51,52]

The parameters σ and v_{th} are the recombination cross section and the thermal velocity, respectively, and N_{to} is the recombination concentration when $N_A = N_{Ao}$ or $N_D = N_{Do}$ in the expression [42]:

$$N_t(x) = \frac{N_{to}}{2}\left(1 + \frac{N(x)}{N_o}\right) . \qquad (51)$$

In addition, the recombination cross section is represented as a function of temperature by [42]:

$$\sigma = \sigma(300K)\ \left(\frac{300}{T}\right)^b . \qquad (52)$$

Using the constants provided for τ_o, $\sigma(300K)$, and v_{th} in Table 3, N_{to} may be calculated and is also listed. Minority carrier lifetimes represented in Eqs. (48) and (49) are now expressed as functions of impurity concentration as well as temperature.

2.2.6.2 Trap-Assisted Auger (TAA)

Trap-assisted Auger (TAA) [43-47] is distinguished from the band-to-band Auger recombination, because TAA recombination is sensitive to trapping level concentration. As a result, TAA may be sensitive to fabrication processes. This arises in those materials and/or from fabrication processes that use high temperatures in which shallow trap concentration is influenced. The trap concentration model used for TAA is represented by Eq. (51), which was introduced for use with SRH recombination.

The composite recombination model formulated considers that a single trap level contributes to both TAA and SRH recombination [42,48]. This is consistent with the single-level analysis that has been extensively

used in the literature and for which there is ample agreement between experimental data and simulation results. Although this analysis, represented by Eq. (47), was developed using the SRH capture and emission processes, it is reasonable to extend this relationship to include TAA recombination [42,48]. However, in SRH the lowest lifetime is obtained for those cases where the trap level $E_t \sim E_{Fi}$ [40,41], while in TAA it is obtained where $E_t \sim E_c$ in n-type and $E_t \sim E_v$ in p-type [42].

The relationship for hole lifetime in n-type is given by [42,48]:

$$\tau_{pTAA} = \frac{1}{T_p N_{tn} n_n} \tag{53}$$

and for electrons in p-type by

$$\tau_{nTAA} = \frac{1}{T_n N_{tp} p_p} \tag{54}$$

where T_p and T_n are the TAA recombination coefficients for holes and electrons, respectively, and n_n and p_p are the nonequilibrium majority carrier concentrations. Hole and electron recombination coefficients may be represented by the expression [43]:

$$T = \frac{2.23 \times 10^{-26}}{(\varepsilon_r m^*)^2} \frac{E'^{5/2}}{(E_G(T,N)-E')^{3/2} E_G^4(T,N)} \tag{55}$$

where $E' = E_c - E_t$ for holes in n-type and $E' = E_t - E_v$ for electrons in p-type. The quantities ε_r and m^* are the relative dielectric constant and the appropriate effective mass. Eq. (55) predicts that electron recombination increases as $E_t - E_v$ decreases, and is lowest for $E_t - E_v = E_G(T,N)$. A corresponding statement may be made for hole recombination.

2.2.6.3 Band-to-Band Auger (BBA)

A band-to-band Auger process may also be present in silicon, which does not require an intermediate trap level [49,50]. This recombination process takes place in degenerate material and/or under high injection levels. The recombination relationship is given by [42]:

$$R_{BBA} = (B_n n + B_p p)(np - n_{ie}^2) \tag{56}$$

where B_n and B_p are the recombination coefficients for electrons in p-type and holes in n-type, respectively. While the values given for the coefficients in the literature show a significant spread, those listed in Table 3 appear to be the most reasonable.

2.2.6.4 Composite Relationship

The composite relationship is obtained by combining the SRH and TAA recombination rate into Eq. (47) and adding Eq. (56) to the result. In Eq. (47) the hole and electron lifetime, τ_p and τ_n, are obtained in a form that includes SRH and TAA using the form [42,48]:

$$\frac{1}{\tau} = \frac{1}{\tau_{SRH}} + \frac{1}{\tau_{TAA}} \quad , \tag{57}$$

for holes and electrons. This results in the relationship

$$\tau_p(x) = \frac{1}{[T_p(x)n_n(x) + \sigma_p v_{thp}]N_{tn}(x)} \tag{58}$$

for holes in n-type using Eqs. (48) and (53), and

$$\tau_n(x) = \frac{1}{[T_n(x)p_p + \sigma_n v_{thn}]N_{tp}(x)} \tag{59}$$

for electrons in p-type using Eqs. (49) and (54). After Eqs. (58) and (59) are substituted in Eq. (47), the result is represented by $R_{SRH/TAA}$. When R_{BBA} and $R_{SRH/TAA}$ are added, the electron lifetime may be obtained given by

$$\frac{1}{\tau_n} = \left[B_n n_p + B_p p_p + \frac{1}{\dfrac{n_p + n_{ie} e^{(E_t - E_{Fi})/kT}}{[T_p n_p + \sigma_p v_{thp}] N_{tp}} + \dfrac{p_p + n_{ie} e^{-(E_t - E_{Fi})/kT}}{[T_n p_p + \sigma_n v_{thn}] N_{tp}}} \right] p_{pe} \left(1 + \frac{p_{po}}{p_{pe}} + \frac{n_{po}}{n_{pe}} \right) \tag{60}$$

where

$$n_p = n_{po} + n_{pe} \tag{61}$$

and

$$p_p = p_{po} + p_{pe} \tag{62}$$

The subscripts o and e represent equilibrium and excess carrier concentrations, and n_p and p_p represent the total, nonequilibrium electron and hole concentrations, respectively. A similar relationship may be obtained for holes.

2.2.7 Induced Surface Electric Field Due to OCI

The simulation program provides for the option of imposing an immobile charge on the irradiated surface of the solar cell. This charge may be distributed arbitrarily throughout the insulator [53-63]. Nevertheless, from Gauss' law the total charge may be considered to reside at the interface. An aiding field in an n-type surface, which reduces surface recombination and improves the junction collection efficiency,

requires the charge to be positive. This tends to repel minority carrier holes and to produce an electron accumulation layer. The model for this structure is shown in Figure 8.

A number of methods have been used to obtain the relationships for the electric field intensity and the electron accumulation distribution [53-63]. The analysis follows from Poisson's equation for the one-dimensional case

$$\frac{dE_s}{dx} = \frac{q}{\varepsilon}[N_D(x) + p_n(x) - n_n(x)] \quad . \tag{63}$$

The boundary conditions imposed on the solution for E(x) are

$$E_x(0) = \frac{Q_s}{\varepsilon} \tag{64}$$

and

$$E_x(x_2) = 0 \quad . \tag{65}$$

Integrating Eq. (63) results in the relationship for the electric field

$$E_s(x) = \frac{q}{\varepsilon}\int_x^{x_2}[n_n(x) - p_n(x) - N_D(x)]dx \quad . \tag{66}$$

This field component is added to the built-in electric field relationship that is discussed in Section 2.2.7. In Eq. (66) the mimobile surface charge density is given by

$$Q_s = q\int_x^{x_2}[n_n(x) - p_n(x) - N_D(x)]dx \tag{67}$$

and satisfies Gauss' theorem.

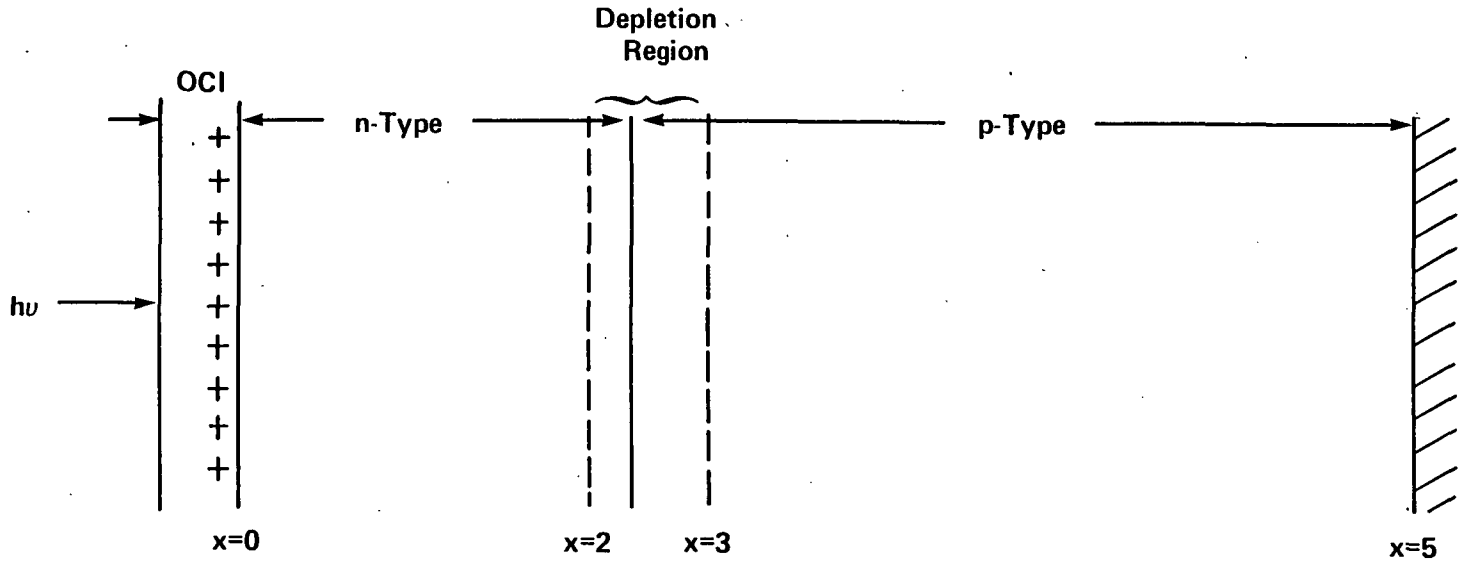

Figure 8. Solar cell structure with immobile charge located at the OCI-semiconductor interface.

A second method may be used to obtain a relationship for the electric field, which is an approximation. The electric field is given by

$$E_s(x) = \frac{Q_s}{\varepsilon} \frac{e^{-\gamma(x)} - e^{-\gamma(x_2)}}{1 - e^{-\gamma(x_2)}} \quad , \tag{68}$$

where

$$\gamma = \frac{q}{Q_s} [n_n(0) - N_o] \quad , \tag{69}$$

for which N_o is the surface donor concentration. The hole concentration does not appear in Eq. (69) because $p_n(0) << N_o$ or $p_n(0) \sim 0$.

2.2.8 Built-in Fields - High and Low Injection Levels

Built-in fields are usually defined as an electrostatic field intensity that exist under thermal equilibrium [64-71]. In treating high injection cases, the intensity of these built-in fields may be markedly affected [72-76]. Moreover, the high injection level may establish another field component that is attributed to photoexcited carriers which is strikingly similar in form to the built-in field that may be present for immobile charge impurities in thermal equilibrium. Therefore, in the following discussion the built-in field label is extended to nonequilibrium cases as well.

The built-in field components will be treated using the ambipolar method [72,73] which may be applied for the entire range of injection levels (i.e., low to high). This approach is the most direct method to illustrate high injection effects on the fields present under equilibrium and nonequilibrium conditions.

The electric field intensity that may be present in the p-type base region is given by

$$E_{pj} = E_{p\Omega j} + E_{pBNj} + E_{plPj} + E_{pPEj} \quad , \tag{70}$$

where

$$E_{p\Omega j} = \frac{b_{pj} J_1}{q\mu_{nj}\Gamma_{pj}} \quad , \tag{71}$$

$$E_{pBNj} = (b_{pj} - \xi_p)\frac{n_{poj}}{\Gamma_{pj}} E_{pBNoj} \quad , \tag{72}$$

$$E_{pBNoj} = -\frac{kT}{q}\frac{2}{n_{iej}}\frac{dn_{iej}}{dx} \quad , \tag{73}$$

$$E_{pIPj} = \left[(b_{pj} - \xi_p)\frac{n_{poj}}{\Gamma_{pj}} + \xi_p \frac{N_{Aj}}{\Gamma_{pj}}\right] E_{pIPoj} \quad , \tag{74}$$

$$E_{pIPoj} = \frac{kT}{q}\frac{1}{N_{Aj}}\frac{dN_{Aj}}{dx} \quad , \tag{75}$$

$$E_{pPEj} = -\frac{kT}{q}\frac{b_{pj} - \xi_p}{\Gamma_{pj}}\frac{dn_{pej}}{dx} \quad , \tag{76}$$

$$\Gamma_{pj} \equiv (b_{\mu j} + \xi_p)n_{pj} + \xi_p N_{Aj} \quad , \tag{77}$$

$$b_{pj} \equiv \frac{F_{1/2}(-\varepsilon_{Gj}-\eta_j)}{F_{-1/2}(-\varepsilon_{Gj}-\eta_j)} \quad , \tag{78}$$

$$b_{\mu j} \equiv \frac{\mu_{nj}}{\mu_{pj}} \quad , \tag{79}$$

$$J_1 = J_n(x) + J_p(x) \quad . \tag{80}$$

Each of the field components in Eq. (70) and the parameters given in Eqs. (71) to (79) are identified by the subscript j, which denotes the j^{th} mesh point. Each is evaluated at the identified mesh point. In Eq. (70),

$E_{p\Omega j}$ represents the field required to conduct the total current (J_1), E_{pBNj} is the electric field present in nonequilibrium and E_{pBNoj} in equilibrium attributed to bandgap narrowing, E_{pIPj} is the field present in nonequilibrium and E_{pIPoj} in equilibrium due to the impurity concentration profile, and E_{pPEj} is the field established by the distribution of photo-excited minority carrier electrons.

Eq. (70) is obtained from a bipolar carrier treatment, where the drift and diffusion components of both electron and hole current contributions are added. Solving for E_{pj} and substituting for p_p from the charge neutrality condition results in Eq. (70). The value of the parameter $\xi_p = 1$ when the ambipolar treatment is required for high injection level, and $\xi_p = 0$ for low level injection.

Eqs. (72), (74), and (76) contain Γ_{pj} in their denominators. Under high injection conditions, $n_{pj}(= n_{poj} + n_{pej}) >> N_{Aj}$, the field components E_{pBNj} and E_{pIPj} decrease with increasing n_{pj}, and when n_{poj}/Γ_{pj}, $N_{Aj}/\Gamma_{pj} << 1$, they are negligible compared to $E_{p\Omega j}$ and E_{pPEj}. It is clear that the field components, E_{pBNoj} and E_{pIPoj}, that are present in thermal equilibrium do not play a major role under high injection levels. With increasing injection level, the ohmic field component, $E_{p\Omega j}$, ultimately approaches a constant value and E_{pPEj} approaches an asymptotical value because $\Gamma_{pj} \rightarrow b_{\mu j} n_{pej}$.

Phenomenologically, the reduction in the role of E_{pBNj} and E_{pIPj} may be understood by associated high injection conditions in a semiconductor with that of metallic-like behavior. Under these conditions, a built-in field established by the distribution of impurities and their effect on the bandgap affects the slope of the conduction and/or valence bandedges. There is a tendency to neutralize these field components

because high current values cannot be supported. Therefore, the high concentration of electrons and holes neutralize these field components. On the other hand, in order to support the high terminal currents under high solar concentration, an electric field, $E_{p\Omega j}$, of moderate value must be present. The corresponding voltage that is required to conduct this current is subtracted from the generated photovoltage across the depletion region (x_2, x_3). Thus, this field is self-limiting and the terminal current cannot increase without limit. Similarly, the electric-field, E_{pPEj}, is also self-limiting, approaching an asymptotic value.

3.0 SUMMARY

The general method to solve the transport equations is discussed. A number of the more important phenomena submodels are presented, and the reasons for selecting the particular form are discussed.

REFERENCES

1. T. Wada and J. Frey, IEEE Trans. Electron Devices, ED-26, 476-90, 1976.

2. M. F. Lamorte and D. H. Abbott, "AlGaAs/GaAs Cascade Solar Cell Computer Modeling Under High Solar Concentration," Solar Cells, 9, 311-326, 1983.

3. M. F. Lamorte and D. H. Abbott, "Influence of Bandgap Span on Cascade Solar Cell Efficiency," Solar Cells, 10, 33-48, 1983.

4. M. F. Lamorte and D. H. Abbott, "Window Losses and Current Mismatch Computer Modeling Studies in AlGaAs-GaAs Cascade Solar Cells," IEEE Trans. Electron Devices, ED-30, 1313-1322, 1983.

5. M. F. Lamorte and D. H. Abbott, "Cascade Solar-Cell Design for High-Temperature Operation," IEEE-Trans. Electron Devices, ED-27, 831-40, 1980.

6. M. F. Lamorte and D. H. Abbott, "Computer Modeling of a Two-junction Monolithic Cascade Solar Cell," IEEE Trans. Electron Devices, ED-27, 231-249, 1980.

7. M. F. Lamorte and D. H. Abbott, "Analysis of AlGaAs-GaInAs Cascade Solar Cell Under AM0-AM5 Spectra," Solid-State Electron, 22, 467-473, 1979.

8. M. F. Lamorte and D. H. Abbott, Final Report No. AFWAL-TR-81-1016: III-V Detector Modeling, March 1981, WPAFB Contract No. F33615-79-C-1828.

9. M. F. Lamorte and D. H. Abbott, Final Report No. AFAL-TR-77-74: Solar Cell Design Study, May 1977, WPAFB Contract No. F33615-76-C-1283.

10. J. M. Dorkel and Ph. Leturcq, Solid-State Electronics, 24, 821-825, 1981.

11. N. D. Arora, J. R. Hauser, and D. J. Roulston, IEEE Trans. Electron Devices, ED-29, 292-295, 1982.

12. J. S. Blakemore, Semiconductor Statistics, Pergamon Press, N.Y., 1962.

13. T. Misawa, J. Phys. Soc. Japan, 11, 728-739, 1956.

14. N. H. Fletcher, J. Electronics, 2, 609-610, 1957.

15. N. H. Fletcher, Proc. IRE, 45, 862-872, 1957.

16. K. M. VanVliet, Solid-State Electronics, 9, 185-201, 1966.

17. H. K. Gummel, Solid-State Electronics, 10, 209-212, 1967.

18. A. Nussbaum, Solid-State Electronics, 12, 177-183, 1969.

19. J. R. Hauser, Solid-State Electronics, 14, 133-139, 1971.

20. E. O. Kane, Phys. Rev., 131, 79, 1963.

21. T. N. Morgan, Phys. Rev., 139, A343, 1965.

22. V. L. Bonch-Bruyevich, The Electronic Theory of Heavily Doped Semiconductors, Elsevier, Amsterdam, 1966.

23. A. A. Vol'fson and V. K. Subashiev, Sov. Physics-Semiconductors, 1, 327, 1967.

24. W. L. Kauffman and A. A. Bergh, IEEE Trans. on Electron Devices, ED-15, 732, 1968.

25. D. Buhanan, IEEE Trans. on Electron Devices, ED-16, 117, 1969.

26. H. J. DeMan, IEEE Trans. on Electron Devices, ED-18, 833, 1971.

27. J. W. Slotboom and H. C. de Graaff, Solid-State Electronics, 19, 857-862, 1976.

28. P. Schmid, M. Thewalt, and W. P. Dunike, Solid-State Commun., 38, 1091, 1981.

29. W. P. Dunike, J. Appl. Phys., 54, 3200-3202, 1983.

30. D. D. Kleppinger and F. A. Lindholm, Solid-State Electronics, 14, 407, 1971.

31. H. J. DeMan, IEEE Trans. Electron Devices, ED-18, 833, 1971.

32. R. VanOverstraeten, H. DeMan, and R. Mertens, IEEE Trans. Electron Devices, ED-20, 290, 1973.

33. H. E. J. Wulms, Solid-State Circuits, SC-12, 143, 1977.

34. H. Heimeier and H. Berger, Solid-State Circuits, SC-12, 205, 1977.

35. R. VanOverstraeten and W. Nuyts, J. Appl. Phys., 43, 4040, 1972.

36. P. Lauwers, J. VanMeerbergen, P. Bulteel, R. Mertens, and R. VanOverstraeten, Solid-State Electronics, 21, 747-752, 1978.

37. G. G. MacFarlane, J. P. McLean, J. E. Quarrington, and V. Roberts, Phys. Rev., 111, 1245, 1958.

38. D. Kendall, Conf. Physics and Applications of Lithium Diffused Silicon, NASA-Goddard Space Flight Center, Dec. 1969.

39. J. G. Fossum, Solid-State Electronics, 19, 269-277, 1976.

40. R. N. Hall, Phys. Rev., 87 387, 1952.

41. W. Shockley and W. T. Read, Jr., Phys. Rev., 87, 835-841, 1952.

42. M. S. Tyagi and R. VanOverstraeten, Solid-State Electronics, 26, 577-597, 1983.

43. P. T. Landsberg, D. A. Evans, and C. Rhys-Roberts, Proc. Phys. Soc., 83, 325, 1964.

44. P. T. Landsberg, D. A. Evans, and C. Rhys-Roberts, Proc. Phys. Soc., 84, 915, 1964.

45. P. T. Landsberg, Phys. Stat. Sol., 41, 457, 1970.

46. P. T. Landsberg and D. J. Robbins, Solid-State Electronics, 21, 1289, 1978.

47. D. J. Robbins and P. T. Landsberg, J. Phys. C: Solid State Phys., 13, 2425, 1980.

48. J. G. Fossum, R. P. Mertens, D. S. Lee, and J. F. Nijs, Solid-State Electronics, 26, 569-576, 1983.

49. A. R. Beattie and P. T. Landsberg, Proc. Roy. Soc., A.249, 16, 1958.

50. P. T. Landsberg and A. R. Beattie, J. Phys. Chem. Solids, 8, 73, 1959.

51. J. Dziewior and W. Schmid, Appl. Phys. Lett., 31, 346-348, 1977.

52. M. S. Adler, IEEE Trans. Electron Devices

53. G. C. Salter and R. E. Thomas, Solid-State Electronics, 20, 95-104, 1977.

54. C. E. Norman and R. E. Thomas, IEEE Trans. Electron Devices, ED-27, 731-737, 1980.

55. G. Baccarani and M. R. Wordman, IEEE Trans. Electron Devices, ED-30, 1295-1304, 1983.

56. Y. C. Ruan and J. Q. Tang, J. Appl. Phys., 55, 1224-1225, 1984.

57. R. H. Kingston and S. F. Neustadter, J. Appl. Phys., 26, 718-720, 1955.

58. C. G. B. Garrett and W. H. Brattain, Phys. Rev., 99, 376-387.

59. A. Neugroschel, F. A. Lindholm, and S. C. Pao, Appl. Phys. Lett., 33, 168-170, 1978.

60. O. von Roos and B. Anspaugh, 13th IEEE Photovoltaic Specialists Conf., Washington, D.C., June 5-8, 1978.

61. F. A. Lindholm, A. Neugroschel, S. C. Pao, J. G. Fossum, and C. T. Sah, 13th IEEE Photovoltaic Specialists Conf., Washington, D.C., June 5-8, 1978.

62. R. J. Schwartz, J. L. Bouknight, and M. S. Worley, Intermt. IEEE Electron Devices Conf., Washington, D.C., December 4-6, 1978.

63. J. L. Gray, R. J. Schwartz, M. S. Lundstrom, and R. D. Nasky, 16th IEEE Photovoltaic Specialists Conf., San Diego, Cal., Sept. 27-30, 1982.

64. B. Dale and F. P. Smith, J. Appl. Phys., 32, 1377-1381, 1961.

65. M. Wolf, Proc. IEEE, 51, 674-693, 1963.

66. S. Kaye and G. P. Rolik, IEEE Trans. Electron Devices, ED-13, 563-570, 1966.

67. W. M. Bullis and W. R. Runyan, IEEE Trans. Electron Devices, ED-14, 75-81, 1967.

68. H. J. J. DeMan, IEEE Trans. Electron Devices, ED-18, 833-835, 1971.

69. R. VanOverstraeten and W. Nuyts, IEEE Trans. Electron Devices, ED-16, 632-641, 1969.

70. S. J. Fonash, CRC Critical Reviews in Solid State and Materials Sciences, 9, 107-209, 1980.

71. Y. Martaing and J. Chevallier, IEEE Trans. Electron Devices, ED-18, 465-471, 1971.

72. W. Z. Shen and C. Y. Wu, Solid-State Electronics, 24, 1025-1037, 1981.

73. W. Z. Shen and C. Y. Wu, J. Appl. Phys., 51, 466-473, 1980.

74. B. L. Grung, Solid-State Electronics, 22, 755-760, 1979.

75. R. P. Mertens, J. F. Nijs, R. J. VanOverstraeten, and S. C. Jain, IEEE Trans. Electron Devices, 29, 922-928, 1982.

76. R. J. Schwartz and M. S. Lundstrom, 14th IEEE Photovoltaic Specialists Conf., San Diego, Calif., Jan. 7-10, 1980.